Acta Materialia 136 (2017) 262–270

Contents lists available at ScienceDirect

Acta Materialia

journal homepage: www.elsevier.com/locate/actamat

Full length article

Ab initio assisted design of quinary dual-phase high-entropy alloys with transformation-induced plasticity

Zhiming Li [a, *], Fritz Körmann [a, b, **], Blazej Grabowski [a], Jörg Neugebauer [a], Dierk Raabe [a]

[a] Max-Planck-Institut für Eisenforschung, Max-Planck-Str. 1, 40237, Düsseldorf, Germany
[b] Delft University of Technology, Mekelweg 2, 2628 CD, Delft, Netherlands

ARTICLE INFO

Article history:
Received 1 April 2017
Received in revised form
13 June 2017
Accepted 10 July 2017
Available online 11 July 2017

Keywords:
High-entropy alloys
Ab initio calculation
Phase transformations
Dual-phase
Mechanical properties

ABSTRACT

We introduce a new class of high-entropy alloys (HEAs), i.e., quinary (five-component) dual-phase (DP) HEAs revealing transformation-induced plasticity (TRIP), designed by using a quantum mechanically based and experimentally validated approach. *Ab initio* simulations of thermodynamic phase stabilities of $Co_{20}Cr_{20}Fe_{40-x}Mn_{20}Ni_x$ (x = 0–20 at. %) HEAs were performed to screen for promising compositions showing the TRIP-DP effect. The theoretical predictions reveal several promising alloys, which have been cast and systematically characterized with respect to their room temperature phase constituents, microstructures, element distributions and compositional homogeneity, tensile properties and deformation mechanisms. The study demonstrates the strength of ab initio calculations to predict the behavior of multi-component HEAs on the macroscopic scale from the atomistic level. As a prototype example a non-equiatomic $Co_{20}Cr_{20}Fe_{34}Mn_{20}Ni_6$ HEA, selected based on our ab initio simulations, reveals the TRIP-DP effect and hence exhibits higher tensile strength and strain-hardening ability compared to the corresponding equiatomic CoCrFeMnNi alloy.

1. Introduction

The concept of high-entropy alloys (HEAs) is of high interest due to its inherent immense compositional variability for designing novel materials with interesting or even undiscovered properties. HEAs were originally proposed to contain multiple principal elements in equimolar or near-equimolar ratios with maximized configurational entropy to stabilize single-phase structures [1–3]. Following this concept, many types of single-phase HEAs have been developed with different crystal structures such as face-centered cubic (FCC) [4,5], body-centered cubic (BCC) [6] and hexagonal close-packed (HCP) [7]. Particularly, the CoCrFeMnNi HEA with single FCC phase at room temperature exhibits excellent mechanical properties under various temperatures [5,8,9]. More recently, based on the fact that maximized configurational entropy is not the sole factor to determine phase stability of HEAs [8,10–14], and due to the demand for further improving mechanical properties of HEAs, a novel design strategy has been proposed to introduce the transformation-induced plasticity (TRIP) effect into HEAs [15,16]. The resulting alloys consist of a high-entropy dual-phase (DP) structure and reveal both, exceptional strength and ductility [15]. The new alloys combine the massive substitutional solid-solution strengthening effect inherent in HEAs with the TRIP effect known from certain high strength steels [17–19]. This leads to improved strength and ductility compared to the above-mentioned single-phase HEAs. However, the new alloy design concept, i.e., TRIP-DP-HEAs, have so far only been realized for the quaternary FeMnCoCr system. Hence, it is promising to explore also quinary systems with more components and presumably larger solid-solution strengthening which can undergo TRIP. However, a purely experimentally based approach is too cumbersome due to the immense compositional space that would need to be screened for identifying suited compositions. Computer simulations are thus required to narrow down the large composition space to such promising target alloys that have a metastability sufficient for exhibiting the TRIP effect.

The TRIP phenomenon is mainly determined by the value of the stacking fault energy (SFE), i.e. the energy carried by the interruption of the normal stacking sequence [20–22]. The SFE is a key atomistic quantity determining whether a material reveals transformation or twinning induced plasticity (TWIP) [17,18,23,24]. A

* Corresponding author.
** Corresponding author. Max-Planck-Institut für Eisenforschung, Max-Planck-Str. 1, 40237, Düsseldorf, Germany.
E-mail addresses: zhiming.li@mpie.de (Z. Li), f.h.w.kormann@tudelft.nl (F. Körmann).

http://dx.doi.org/10.1016/j.actamat.2017.07.023
1359-6454/

low SFE results into decreased cross-slip and dislocation climb [25,26]. It also can affect the dislocation core properties and hence influence their mobility. The SFE, which is related to the thermal HCP-FCC phase stability [15,25], is directly accessible by both atomistic simulations and experimental measurements [20,27]. Therefore it is a central quantity linking theory and experiment. Challenges associated with SFE simulations for HEAs are that: i) small changes of the order of a few ~ mJ/m^2 can be decisive for the dominant deformation mechanism (TRIP vs. TWIP) [27], ii) SFEs are strongly temperature dependent [28], and iii) the large configuration space due to the inherent multi-element character of HEAs.

Ab initio simulations, in particular density functional theory (DFT) calculations, provide an attractive tool to screen the large compositional space of HEAs [3,29]. A number of DFT studies have been performed for HEAs in the last years, however, mainly focusing on ground state properties at zero temperature such as equilibrium volumes or elastic properties [30–33]. Only a few SFE DFT calculations have been reported so far. Zaddach et al. [34] investigated SFEs for a number of alloys ranging from pure Ni to CoCrFeMnNi based on DFT derived elastic constants at 0 K in combination with experimental input, revealing the tunability of SFEs through alloy composition. An SFE of ~20–30 mJ/m^2 for the CoCrFeMnNi alloy has been reported [34].

Finite-temperature ab initio predictions have been published [14] for the CoCrFeMnNi alloy revealing the importance of various entropy contributions (e.g., magnetic fluctuations and lattice excitations). Huang et al. [35] performed a DFT based finite-temperature SFE study for the CoCrFeMnNi alloy taking lattice expansion from experimental data and magnetism fluctuations within a mean field treatment into account [35]. Thermal induced lattice vibrations, which were found to affect the phase stability of such alloys [14], have, however, so far not been included in finite-temperature ab initio SFE simulations for such alloys.

The main aim of this work is to introduce the recently proposed "TRIP-DP" concept for quaternary $Fe_{50}Mn_{30}Co_{10}Cr_{10}$ [15] also into quinary CoCrFeMnNi HEAs by coupling theoretical simulations and experimental investigations. For this purpose we have employed DFT calculations to screen for promising alloys with SFEs and HCP-FCC phase stabilities in $Co_{20}Cr_{20}Fe_{40-x}Mn_{20}Ni_x$ alloys (x = 0–20 at. %) that fall in a regime where deformation-driven phase transformation is promoted. Based on the DFT simulations we have predicted several alloys, which were then synthesized and their microstructure-mechanical property relations were studied to validate the feasibility of the here proposed theory-assisted alloy design approach.

2. Methodology

2.1. Finite temperature ab initio calculations

DFT calculations were performed employing the exact muffin-tin orbitals (EMTO) method [36–39]. Chemical disorder was taken into account via the coherent potential approximation (CPA) [38,40,41] within an effective 1-atomic unit cell. For the self-consistent electronic density calculations we employed the generalized gradient approximation (GGA) [42]. The Brillouin zone integration was done based on a 45 × 45 × 45 and 45 × 45 × 27 k-point mesh for FCC and HCP according to the Monkhorst–Pack scheme [43]. For the HCP structure an ideal c/a ratio of $\sqrt{8/3}$ has been employed. Other parameters were set as outlined in Ref. [14]. A ferrimagnetic state with Mn and Cr antiferromagnetically aligned to ferromagnetic Fe, Co and Ni is found at 0 K [14]. As the Curie temperature is well below room temperature (see, e.g., [44]), all simulations were performed in the paramagnetic state. The paramagnetic state was modeled employing the disordered local moment (DLM) model [45,46].

In order to evaluate the impact of finite-temperature effects, lattice vibrations were included via the Debye model within the harmonic approximation in which the volume is kept fixed [47]. The Debye temperature, θ_D, has been computed based on the Moruzzi approach [47] as $\theta_D = C\sqrt{(3V_0/4\pi)^{1/3}B_0/M}$, where C = 41.64 is an empirical constant, V_0 is the equilibrium volume and B_0 is the bulk modulus. Magnetic fluctuations were treated within a mean field approach as described in Refs. [14,35]. Further technical details are given in Ref. [14].

2.2. Experimental methods

2.2.1. Alloy processing

The ingots of the three alloys, namely $Co_{20}Cr_{20}Fe_{20}Mn_{20}Ni_{20}$, $Co_{20}Cr_{20}Fe_{34}Mn_{20}Ni_6$ and $Co_{20}Cr_{20}Fe_{40}Mn_{20}$ (all in at. %) with the same dimensions of 25 × 60 × 65 mm^3 were cast in a vacuum induction furnace using cleaned pure metals (>99.8% pure) to predetermined nominal compositions. Samples with dimensions of 10 × 25 × 60 mm^3, machined from the original cast, were subsequently hot-rolled at 900 °C to a thickness reduction of 50% (thickness changed from 10 to 5 mm). After hot-rolling, the samples were homogenized at 1200 °C for 2 h in Ar atmosphere followed by water-quenching.

2.2.2. Microstructural and elemental characterization

The microstructures of the alloys in the homogenized state were analyzed using various methods. We subjected the homogenized alloys for analysis to avoid any microstructure and deformation effects arising from compositional inhomogeneity [48]. X-ray diffraction (XRD) measurements were performed using an X-Ray equipment ISO-DEBYEFLEX 3003 equipped with Co Kα (λ = 1.788965 Å) radiation operated at 40 kV and 30 mA. Electron backscatter diffraction (EBSD) measurements were carried out by a Zeiss-Crossbeam XB 1540 FIB scanning electron microscope (SEM) with a Hikari camera and the TSL OIM data collection software. Back-scattered electron imaging (BSEI) and electron channeling contrast imaging (ECCI, [49]) analyses were performed on a Zeiss-Merlin instrument. The grain sizes of the FCC matrix in the homogenized alloys were calculated from multiple BSE images and EBSD maps by the intercept method. The calculation of the FCC grain size was based on the whole FCC matrix grain which may contain HCP laminate phase in the case of the dual-phase HEAs [19]. The bulk chemical compositions of the three alloys were measured by wet-chemical analysis. The elemental distributions in the homogenized alloys were investigated using energy-dispersive X-ray spectroscopy (EDS) at microscale and atom probe tomography (APT) (LEAP 3000X HR, Cameca Inc.) at nanoscale. Site-specific lift-out of APT tips was performed from the regions including phase and grain boundaries (revealed by a prior EBSD scan) using the focused ion beam (FIB) technique (FEI Helios Nanolab 600i) [15,19].

Prior to the microstructural analysis, fine polishing of the sample surfaces was performed for more than half an hour using an oxide suspension (OPS) with silica particle sizes around 50 nm to effectively remove the deformation layer caused by mechanical grinding. The sample surfaces were finally polished for 2–3 min using ethanol to remove the nano-silica particles.

2.2.3. Mechanical characterization

Rectangular dog-bone-shaped specimens for tensile testing, with a thickness of 1 mm, were machined from the alloy sheets in the homogenized state by electrical discharge machining. The gauge length and width of the tensile specimens were 10 and 2.5 mm, respectively. Uniaxial tensile tests were performed using a Kammrath & Weiss tensile stage at an engineering strain rate of

1×10^{-3} s^{-1}. Three samples for each homogenized alloy were tensile tested at room temperature (293 K). The local strain evolution during tensile testing was determined by digital image correlation (DIC) method using Aramis system (GOM GmbH). The deformation microstructures in the fractured tensile samples were also investigated by EBSD and ECCI at different regions with different local strain levels.

3. Results and discussion

3.1. Ab initio simulations – phase stability analysis and screening of potential alloys

In our preliminary work [15], the quaternary $Fe_{50}Mn_{30}Co_{10}Cr_{10}$ has been identified as a promising TRIP-DP-HEAs reference composition. In order to screen for potential quinary TRIP-DP-HEAs we employ a combined theoretical-experimental strategy in the present work. In particular, we screen the Fe/Ni compositional ratio in $Co_{20}Cr_{20}Fe_{40-x}Mn_{20}Ni_x$ alloys with x = 0–20 at. %, i.e. from quinary $Co_{20}Cr_{20}Fe_{20}Mn_{20}Ni_{20}$ (Cantor alloy) towards quaternary $Co_{20}Cr_{20}Fe_{40}Mn_{20}$.

DFT simulations employing the EMTO approach [37] (see Sec. 2.1) were used to investigate the HCP-FCC phase stability for 11 different compositions from $Co_{20}Cr_{20}Fe_{20}Mn_{20}Ni_{20}$ to $Co_{20}Cr_{20}Fe_{40}Mn_{20}$, i.e. by considering $Co_{20}Cr_{20}Fe_{40-x}Mn_{20}Ni_x$ with x varying in steps of 2 at. %. Chemical and magnetic disorder were taken into account employing the CPA and DLM methods. Lattice excitations and magnetic entropy effects were included via the harmonic Debye model as well as by a magnetic mean field approach similar as for the quinary alloys [14]. The results are shown in Fig. 1. We first performed all calculations at the theoretical lattice constant of ≈3.52 Å and included finite-temperature contributions at 300 K within the harmonic approximation. A strong compositional dependence is found for the HCP-FCC phase stability on Ni content, revealing enhanced HCP phase stability with reduced Ni concentration (lower black dashed line). Adding finite-temperature contributions reduces the HCP stability for all considered alloy compositions. In particular vibrations (blue dashed line) are found to be important for the phase stability. At 300 K, the HCP phase is found to be stable for all considered alloys, including the $Co_{20}Cr_{20}Fe_{20}Mn_{20}Ni_{20}$ alloy consistent with our previous work [14].

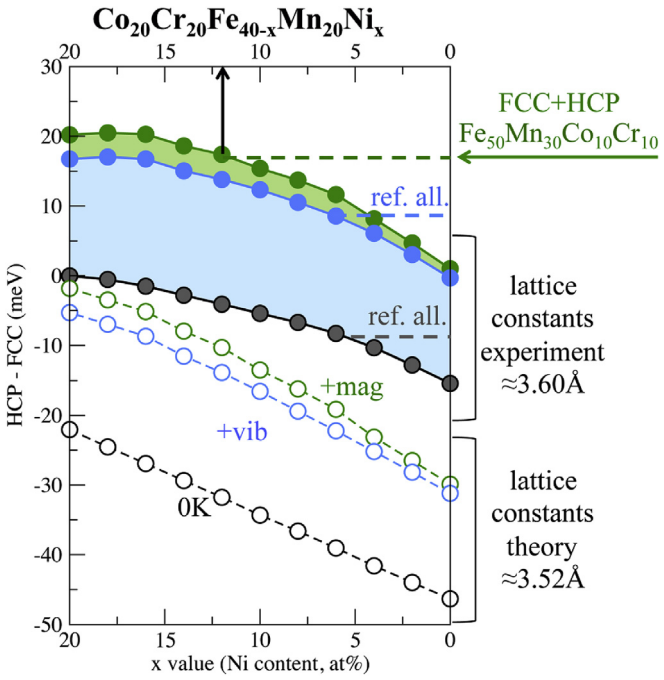

Fig. 1. DFT derived HCP-FCC energy differences for $Co_{20}Cr_{20}Fe_{40-x}Mn_{20}Ni_x$ with varying Ni content of x = 0–20 at 0 K (black), including lattice vibrations (blue) and magnetic entropy effects (green) at 300 K. The thin dashed lines correspond to calculations performed at the theoretical $T = 0$ K lattice constants (≈3.52 Å) whereas the thick lines correspond to simulations carried out at experimental lattice constants (≈3.60 Å). The reference alloy energies are derived for the TRIP-DP-HEA $Fe_{50}Mn_{30}Co_{10}Cr_{10}$ [15]. The largest Ni concentrations predicted by the simulations reveal lower HCP-FCC energy differences as the reference alloy vary between 6 and 12 at. %. (For interpretation of the references to colour in this figure legend, the reader is referred to the web version of this article.)

As the theoretically predicted lattice constants at ambient temperature of ≈3.54 Å are still smaller compared to the experimentally observed ones [50], we performed all calculations using the experimentally determined lattice constant of 3.6 Å for the CoCrFeMnNi alloy as reported in literature [50]. Note that we also determined this lattice parameter for the present alloys by our XRD analysis as discussed below. For all compositions considered, the larger (experimental) lattice constant shifts the HCP-FCC energy differences to larger values i.e. enhancing stability of the FCC phase.

As the simulation results strongly depend on the chosen lattice parameters we employ a reference energy value for the expected TRIP-DP-HEA compositions. For this purpose we derived the Gibbs energy of our reference alloy $Fe_{50}Mn_{30}Co_{10}Cr_{10}$ [15], which reveals the TRIP-DP effect, including the various finite-temperature Gibbs energy contributions. The ground state energy and the Gibbs energies including vibrations as well as magnetic effects are shown in Fig. 1 as dashed grey, blue and green lines, respectively. Promising TRIP-DP-HEA compositions are identified for those Ni-concentrations for which smaller HCP-FCC energy differences are found as for our reference alloy. Our DFT simulations predict the crossing points between the reference alloy and the quinary HEAs at around 12 at. % Ni concentration (6 at. % if magnetic excitations were not included). We therewith anticipate to find promising TRIP-DP alloys starting from $Co_{20}Cr_{20}Fe_{40}Mn_{20}$ up to $Co_{20}Cr_{20}Fe_{40-x}Mn_{20}Ni_x$ alloys containing up to 12 at. %. The analysis reveals once more the importance of thermal excitations for phase stability predictions.

3.2. Microstructure and compositional homogeneity

Following the theoretical investigations we prepared three alloys with Ni content of 20, 6 and 0 at. %, namely $Co_{20}Cr_{20}Fe_{20}Mn_{20}Ni_{20}$, $Co_{20}Cr_{20}Fe_{34}Mn_{20}Ni_6$ and $Co_{20}Cr_{20}Fe_{40}Mn_{20}$. The $Co_{20}Cr_{20}Fe_{20}Mn_{20}Ni_{20}$ HEA was prepared for benchmark studies and to have full control of the experimental setup independent of previous literature data. We have chosen the composition with 6 at. % Ni resulting from a conservative interpretation of our simulation analysis presented above i.e. by choosing the maximum Ni concentration predicted by our simulations independent of the employed treatment of finite-temperature excitations. We produced the $Co_{20}Cr_{20}Fe_{40-x}Mn_{20}Ni_x$ (x = 20 at. %, 6 at. % and 0 at. %) HEAs by melting and casting using pure metals to the predetermined nominal compositions. The bulk chemical compositions of the three HEAs measured by wet-chemical analysis are shown in Table 1.

Fig. 2 shows the XRD patterns of the three homogenized HEAs. When decreasing the Ni content in the $Co_{20}Cr_{20}Fe_{40-x}Mn_{20}Ni_x$ HEA system from 20 at. % to 6 at. %, the structure of the alloys shifts from single FCC phase to dual-phase (FCC and HCP) with ~6 vol% of HCP phase at the homogenized state without strain loading. Note that the initial HCP phase was thermally induced through the displacive transformation during the water-quenching process after high-temperature (1200 °C) homogenization [15,19]. With further decreasing Ni content down to 0%, the initial HCP phase fraction increases to ~69 vol %. This confirms the theoretically derived trend

Table 1
Bulk chemical composition of the homogenized $Co_{20}Cr_{20}Fe_{40-x}Mn_{20}Ni_x$ HEAs in atomic per cent according to wet-chemical analysis and the corresponding average grain size values of the FCC matrix as well as the statistical standard deviations.

Alloy	Co	Cr	Fe	Mn	Ni	FCC matrix grain size, μm
$Co_{20}Cr_{20}Fe_{20}Mn_{20}Ni_{20}$	20.08	20.06	19.98	19.91	19.97	140 ± 14
$Co_{20}Cr_{20}Fe_{34}Mn_{20}Ni_6$	19.84	20.02	34.19	19.97	5.99	130 ± 16
$Co_{20}Cr_{20}Fe_{40}Mn_{20}$	19.97	19.86	39.96	20.21	–	95 ± 13

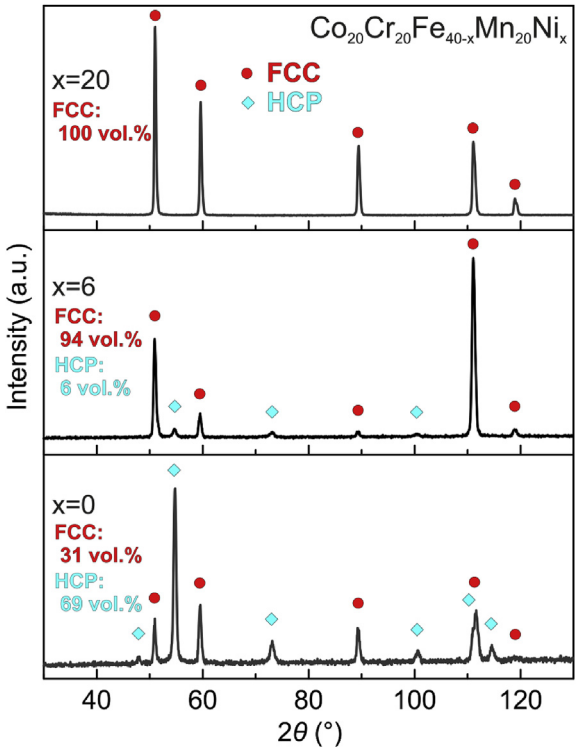

Fig. 2. XRD patterns of homogenized $Co_{20}Cr_{20}Fe_{40-x}Mn_{20}Ni_x$ (x = 20 at. %, 6 at. % and 0) HEAs reveal the variations of phase configurations with changing the x value (Ni content).

predicted above, namely, that the stability of HCP phase increases with decreasing Ni content.

Fig. 3a shows a typical EBSD phase map of the $Co_{20}Cr_{20}Fe_{34}Mn_{20}Ni_6$ alloy, which confirms the dual-phase structure consisting of the FCC and HCP high-entropy phases. The ECCI results in Fig. 3b and c reveal a high density of stacking faults in the FCC phase of the quinary dual-phase HEA after homogenization and water-quenching, indicating a very low SFE of the new alloy. EDS maps in Fig. 2d show that all elements (Co, Cr, Fe, Mn and Ni) are uniformly distributed among the dual-phase structure. There are a few inclusions enriched in Mn with an area fraction of approximately 0.2% according to multiple BSE images and EDS maps. These inclusions are likely sulfides or oxides as commonly observed in high-Mn alloys and steels, including the well-known equiatomic $Co_{20}Cr_{20}Fe_{20}Mn_{20}Ni_{20}$ HEA [5].

To examine the exact local concentration in the quinary alloy excluding the inclusions enriched in Mn and to reveal the elemental distribution at nanometer scale, APT tips were lifted out from the boundary region as indicated in Figs. 3b and 4a. The three-dimensional APT tip reconstruction of all elements in a representative tip (Fig. 4b) shows that there is no observable elemental segregation in the investigated volume. One-dimensional concentration profiles (Fig. 4c) of all the elements shows that there is no apparent fluctuation of elemental fractions along the length direction of the tip, and the analysis reveals that the tip has an overall composition of $Co_{20.82}Cr_{19.26}Fe_{35.46}Mn_{17.59}Ni_{6.87}$ (all in at. %). Furthermore, the statistical binomial frequency distribution analysis (Fig. 4d) shows that the binomial curves obtained from experiments match the curves corresponding to a total random distribution. The values of the normalized homogenization parameter μ for all elements are close to 0, confirming the random distribution of all the elements (Co, Cr, Fe, Mn and Ni).

3.3. Mechanical behavior

Fig. 5a shows the representative tensile stress-strain curves of the quinary dual-phase $Co_{20}Cr_{20}Fe_{34}Mn_{20}Ni_6$ HEA compared to other quaternary and quinary HEAs at identical processing state and similar grain sizes. We observe that the newly developed quinary dual-phase $Co_{20}Cr_{20}Fe_{34}Mn_{20}Ni_6$ HEA has a significantly higher ultimate tensile strength (545 ± 11 MPa) compared to the TWIP-assisted quinary single-phase equiatomic $Co_{20}Cr_{20}Fe_{20}Mn_{20}Ni_{20}$ HEA (400 ± 15 MPa), although they have similar yield strength (155 ± 10 MPa). Also, the ultimate tensile strength of the quinary dual-phase $Co_{20}Cr_{20}Fe_{34}Mn_{20}Ni_6$ HEA is higher than that of the TWIP-assisted quaternary single-phase $Fe_{40}Mn_{40}Co_{10}Cr_{10}$ HEA (495 ± 16 MPa) [8], although the latter one has a little higher yield strength. We also observe that the total elongation of the quinary dual-phase $Co_{20}Cr_{20}Fe_{34}Mn_{20}Ni_6$ HEA (45% ± 3%) is slightly lower than that of the other two quaternary and quinary single-phase HEAs with similar grain sizes shown in Fig. 5a, and is also lower than the total elongation of the quaternary dual-phase $Fe_{50}Mn_{30}Co_{10}Cr_{10}$ HEA with smaller grain size investigated before [15]. Moreover, the quaternary $Co_{20}Cr_{20}Fe_{40}Mn_{20}$ alloy shows significantly decreased total elongation (28% ± 2%), although the ultimate tensile strength (650 ± 17 MPa) is significantly higher than that of the other reference alloys. The significantly lower ductility of the quaternary $Co_{20}Cr_{20}Fe_{40}Mn_{20}$ alloy is due to the very low stability of the FCC phase, which means that the rate of phase transformation is relatively high and hence the transformation capacity will be consumed already at modest strain levels [19].

Fig. 5b reveals the corresponding strain-hardening behavior with respect to the true strain in the same group of alloys. The dual-phase quinary $Co_{20}Cr_{20}Fe_{34}Mn_{20}Ni_6$ and quaternary $Co_{20}Cr_{20}Fe_{40}Mn_{20}$ HEAs show significantly higher strain-hardening rates compared to the quinary single-phase $Co_{20}Cr_{20}Fe_{20}Mn_{20}Ni_{20}$ HEA over the entire plastic deformation process. Also, compared to the TWIP-assisted quaternary single-phase $Fe_{40}Mn_{40}Co_{10}Cr_{10}$ HEA [8], the quinary dual-phase $Co_{20}Cr_{20}Fe_{34}Mn_{20}Ni_6$ HEA shows much higher strain-hardening rates at the medium and later deformation stages with true strain values higher than 15%. This suggests that the deformation mechanisms triggered in the quinary dual-phase $Co_{20}Cr_{20}Fe_{34}Mn_{20}Ni_6$ HEA have higher capability to induce strain-hardening, hence leading to higher ultimate tensile strength.

3.4. Microstructural evolution upon deformation

The significant improvement of ultimate tensile strength and strain-hardening rate of the quinary dual-phase $Co_{20}Cr_{20}Fe_{34}Mn_{20}Ni_6$ HEA compared to other single-phase HEAs is

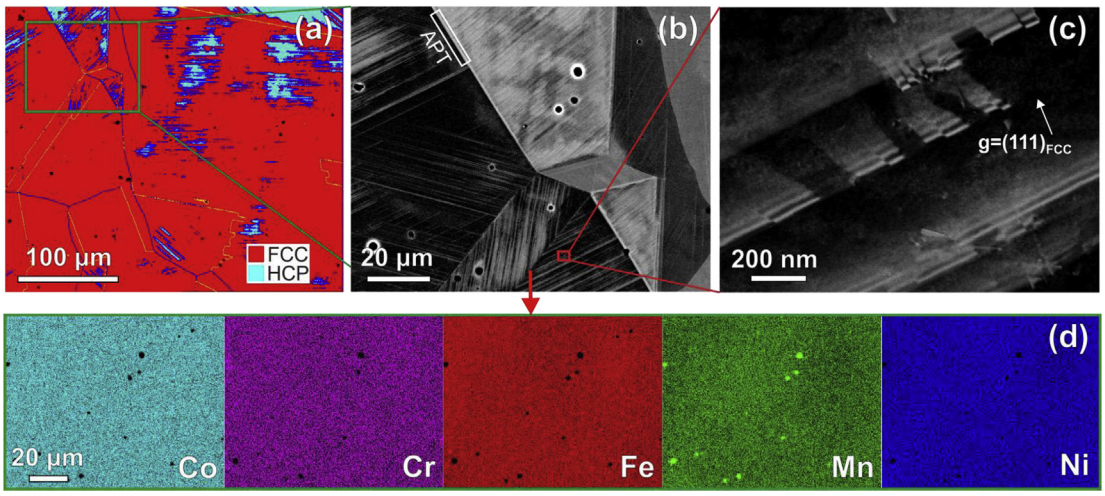

Fig. 3. Microstructure and elemental distribution in the $Co_{20}Cr_{20}Fe_{34}Mn_{20}Ni_6$ HEA in the homogenized state. (a) EBSD phase map confirms the dual-phase structure in the alloy. (b) Low-magnification ECCI results corresponding to the identical region marked in (a). (c) High-magnification ECCI results corresponding to the identical region marked in (b) shows the nano-sized stacking faults in the starting microstructure. (d) EDS maps corresponding to the same region in (b) show that all elements (Co, Cr, Fe, Mn and Ni) are uniformly distributed, although there are a few inclusions enriched with Mn.

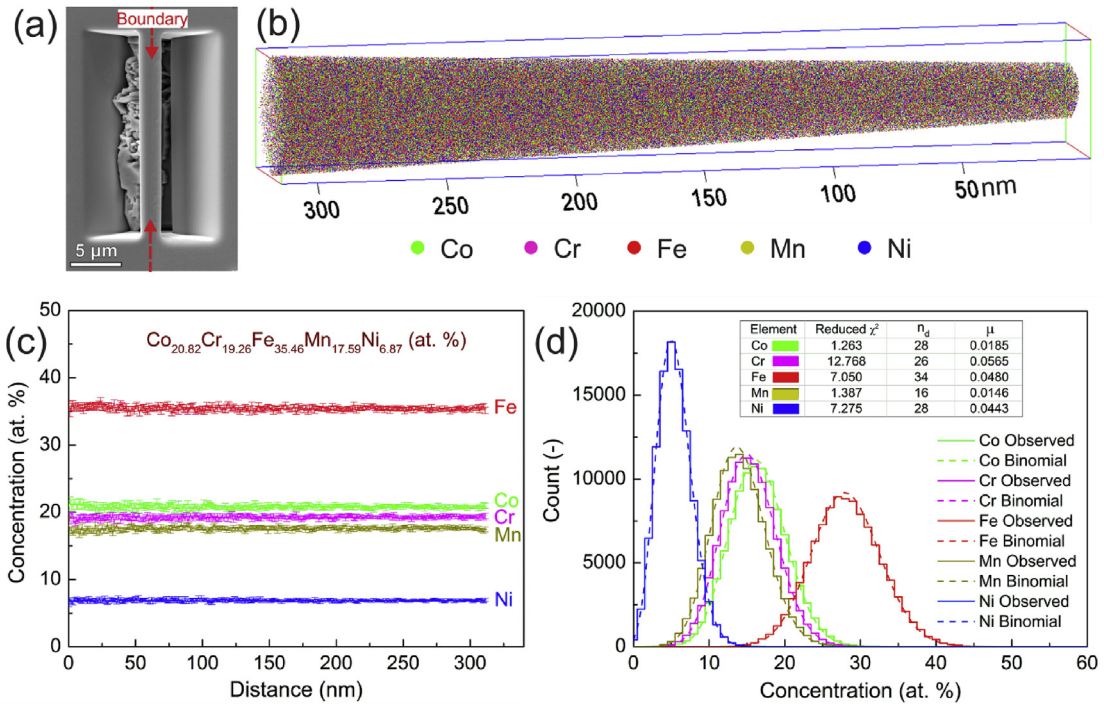

Fig. 4. Representative APT analysis on the homogenized $Co_{20}Cr_{20}Fe_{34}Mn_{20}Ni_6$ HEA. (a) SE image showing the site-specific lift-out by the FIB technique at a boundary also marked in Fig. 3b. (b) Three-dimensional APT tip reconstruction of all elements in one of the tips taken from the boundary region shown in (a). (c) One-dimensional concentration profiles taken along the length direction of the tip shown in (b). (d) Frequency distribution analysis obtained both from observed experimental results and from the binomial simulation. Several parameters were employed to assess the quality of the fit of the experimental results to the binomial simulation, as listed in the inserted table in (d). n_d and μ are the number of degrees of freedom for a given ion and normalized homogenization parameter, respectively.

associated with the strengthening mechanisms active in the new HEA. We reveal this in the following by correlative EBSD (Fig. 6) and ECCI (Fig. 7) analyses. The EBSD phase maps (Fig. 6) show that a martensitic transformation from the FCC to the HCP phase was induced upon strain loading, and acted as a primary deformation mechanism in the bulk quinary dual-phase $Co_{20}Cr_{20}Fe_{34}Mn_{20}Ni_6$ HEA. The average fraction of transformed HCP phase at the necking stage (local strain of ~100%) is ~70% (Fig. 6d), which is near to the value observed in the quaternary dual-phase $Fe_{50}Mn_{30}Co_{10}Cr_{10}$ HEA (~80%) [15]. This is consistent with our current DFT calculations, namely, that the HCP—FCC energy difference in this new quinary dual-phase $Co_{20}Cr_{20}Fe_{34}Mn_{20}Ni_6$ HEA is similar as that in the reference quaternary $Fe_{50}Mn_{30}Co_{10}Cr_{10}$ HEA.

Other than the transformed HCP phase, we also observe high amounts of stacking faults both at the uniform deformation stages (Fig. 7a) and the necking stage (Fig. 7b) from the ECCI analysis conducted on the bulk strained samples. The stacking faults observed in the retained non-transformed FCC phase show similar

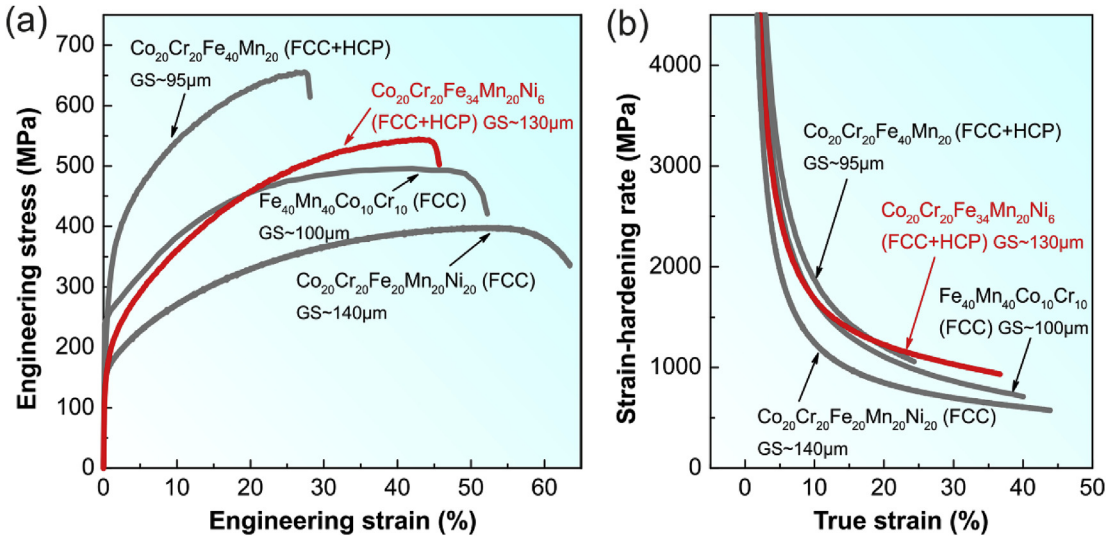

Fig. 5. Mechanical behavior of the quinary dual-phase $Co_{20}Cr_{20}Fe_{34}Mn_{20}Ni_6$ HEA compared to other quaternary and quinary HEAs. GS refers to the grain size. (a) Typical engineering stress-strain curves; all curves are obtained from uniaxial tensile tests with the same testing conditions on the homogenized alloys produced in-house. (b) Strain-hardening for the same group of alloys.

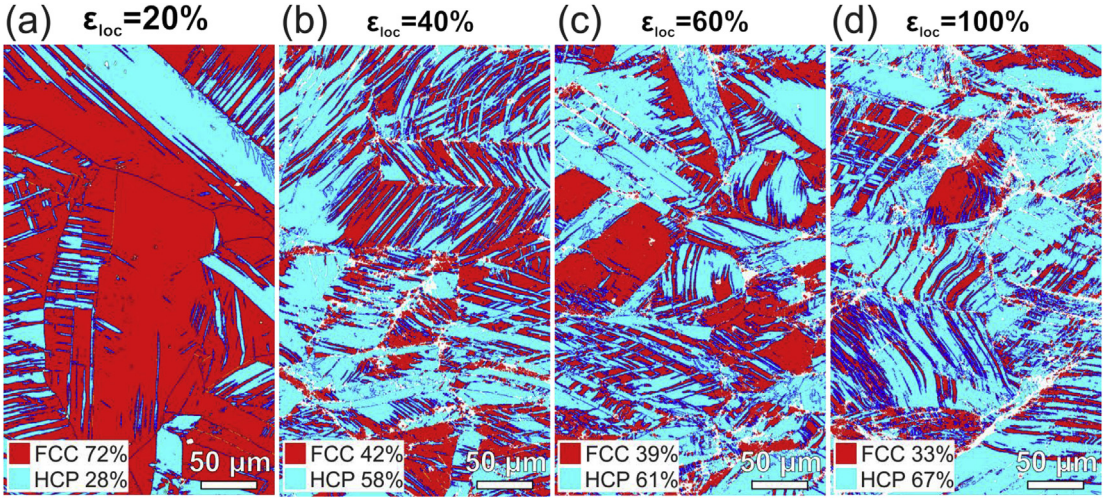

Fig. 6. EBSD phase maps of the quinary dual-phase $Co_{20}Cr_{20}Fe_{34}Mn_{20}Ni_6$ HEA with increasing tensile deformation at room temperature. The results reveal deformation-induced martensitic transformation as a function of deformation; the local strain (ε_{loc}) levels of (a) 20%, (b) 40%, (c) 60% and (d) 90% correspond to the early, medium and late uniform deformation and post-necking stages, respectively.

crystallographic orientation as the newly formed HCP phase (Fig. 7a and b). This is consistent with previous observations made in other FCC-HCP TRIP alloys, namely, that the thin stacking fault plates consisting of only a few several atomic monolayers of HCP structure act as the nuclei of the HCP martensite phase [15,51]. No obvious twinning phenomenon was observed in the homogenized $Co_{20}Cr_{20}Fe_{34}Mn_{20}Ni_6$ HEA upon deformation. This is due to the very low phase stability of the FCC matrix, which leads to the preferential occurrence of displacive phase transformation over mechanical twining. Also, a high density of dislocations can be observed (Fig. 7b), which is essential since the stacking faults in the FCC phase are formed by gliding of Shockley partials [51]. These observations confirm that the new quinary dual-phase $Co_{20}Cr_{20}Fe_{34}Mn_{20}Ni_6$ HEA designed with the assistance of DFT calculations exhibits deformation induced displacive transformation and dislocation plasticity. This observation also explains the significant improvement in ultimate tensile strength and strain-hardening rate of the quinary dual-phase HEA compared to those of other single-phase HEAs, and further proves that the TRIP effect is active in the newly designed alloy upon strain loading.

Furthermore, to understand the deformation behavior of the quaternary $Co_{20}Cr_{20}Fe_{40}Mn_{20}$ alloy with the highest HCP phase stability among the probed alloys based on the DFT calculations (Fig. 1), the corresponding microstructural evolution has also been investigated and the results are shown in Fig. 8. Analogous to the newly designed quinary $Co_{20}Cr_{20}Fe_{34}Mn_{20}Ni_6$ HEA, the quaternary $Co_{20}Cr_{20}Fe_{40}Mn_{20}$ alloy also exhibits a dual-phase structure consisting of a FCC high-entropy phase and a coexisting HCP high-entropy phase. However, the initially available HCP phase fraction prior to deformation in the quaternary $Co_{20}Cr_{20}Fe_{40}Mn_{20}$ HEA (69% from XRD in Fig. 2 and 61% from EBSD in Fig. 8) is significantly higher than that observed in the quinary alloy (6% from XRD in

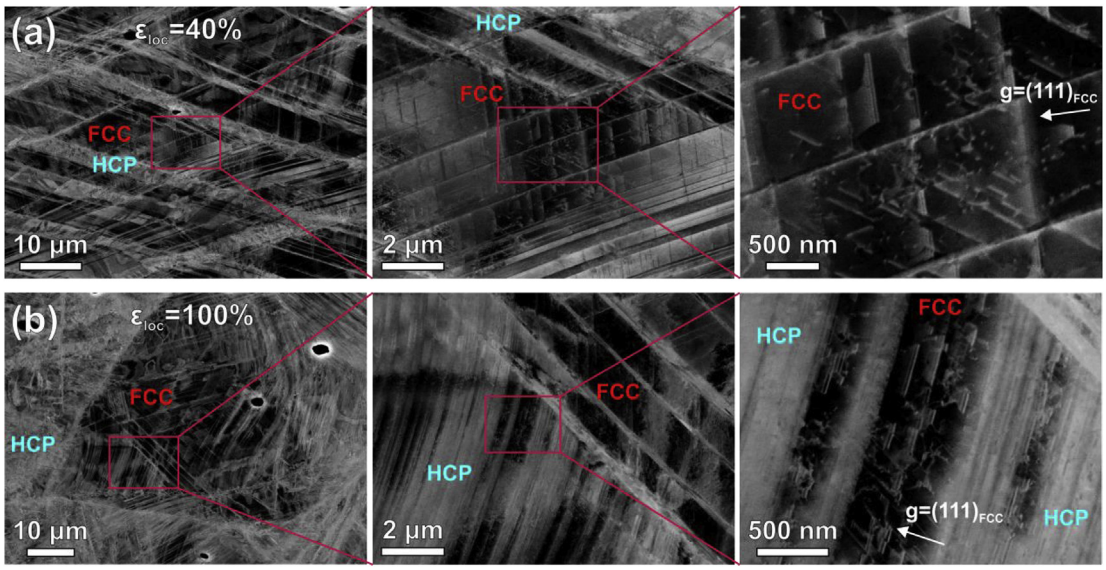

Fig. 7. ECCI analyses of the quinary $Co_{20}Cr_{20}Fe_{34}Mn_{20}Ni_6$ HEA revealing deformation induced HCP phase, stacking faults and dislocations at the local strain levels of (a) 40% and (b) 100%, respectively.

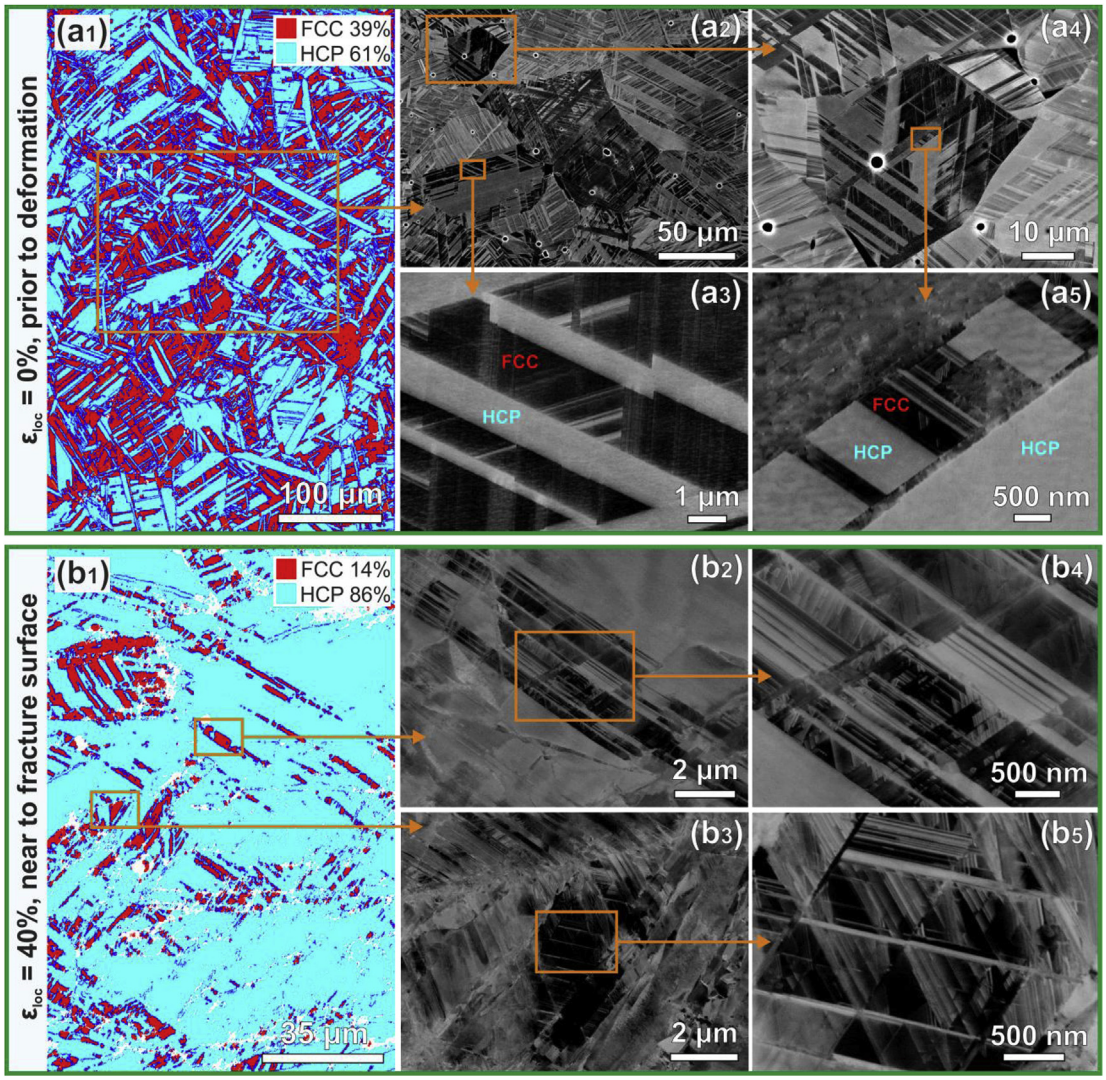

Fig. 8. Typical EBSD phase maps (a_1 and b_1) and ECC images ($a_{2\text{-}5}$ and $b_{2\text{-}5}$) obtained on the quaternary $Co_{20}Cr_{20}Fe_{40}Mn_{20}$ alloy at local strain (ε_{loc}) levels of ($a_{1\text{-}5}$) 0% and ($b_{1\text{-}5}$) 40%, revealing the microstructural evolution upon deformation. The local strain levels of 0% and 40% refer to the sample regions without deformation and near to the fracture surface, respectively.

Fig. 2), which is the main reason for the higher yield strength of the quaternary alloy (Fig. 5). The ECC images in Fig. 8$a_{2\text{-}5}$ clearly show a high amount of laminate HCP phase with a width varying from the submicron scale up to several micrometers. The HCP laminates with widths below 50 nm could not be captured by EBSD, which explains the higher HCP fraction obtained by XRD than by EBSD [19]. After tensile deformation to a local strain level of 40% which corresponds to the stage prior to fracture of this alloy, the HCP phase fraction increased to 86% according to EBSD analysis (Fig. 8b_1). From the ECCI analysis (Fig. 8$b_{2\text{-}5}$), a very high density of stacking faults can be observed even in the remaining FCC phase regions. These results suggest that displacive transformation from the FCC to HCP phase and the formation of stacking faults are the prevalent deformation mechanisms in this quaternary $Co_{20}Cr_{20}Fe_{40}Mn_{20}$ alloy.

The results discussed above reveal that the newly developed dual-phase quinary $Co_{20}Cr_{20}Fe_{34}Mn_{20}Ni_6$ and quaternary $Co_{20}Cr_{20}Fe_{40}Mn_{20}$ HEAs show much higher tensile strength and strain-hardening ability compared to the corresponding equiatomic $Co_{20}Cr_{20}Fe_{20}Mn_{20}Ni_{20}$ alloy due to the successful introduction of a TRIP-DP effect. However, the quaternary $Co_{20}Cr_{20}Fe_{40}Mn_{20}$ HEA shows significantly lower ductility than the quinary $Co_{20}Cr_{20}Fe_{34}Mn_{20}Ni_6$ HEA due to the further decreased FCC phase stability and hence the correspondingly increased HCP phase stability. This finding suggests that, for achieving a good strength-ductility combination, the phase stability of the alloys should be tuned into a proper regime where the FCC phase stability in the CoCrFeMnNi system is not too low as this may lead to premature phase transformation and thus low ductility. Besides using a substitutional alloying concept for this purpose such as discussed in this work, the FCC phase stability can also be modified via interstitial alloying [16] or by grain size adjustment [19].

4. Conclusions

We introduced a new class of HEAs, i.e., quinary TRIP-DP-HEAs, designed by using a quantum mechanical approach coupled with experiments. *Ab initio* simulations of thermodynamic HCP-FCC phase stabilities of $Co_{20}Cr_{20}Fe_{40\text{-}x}Mn_{20}Ni_x$ (x = 0–20 at. %) HEAs were performed to screen for promising compositions revealing the TRIP-DP effect. Consistent with previous work our simulations revealed the importance of finite-temperature contributions such as vibrations and magnetic fluctuations to the phase stability. Based on the theoretical results we selected and casted several alloys and characterized them with respect to their room temperature phase constituents, microstructures, elemental distributions, tensile properties and deformation mechanisms. The non-equiatomic $Co_{20}Cr_{20}Fe_{34}Mn_{20}Ni_6$ HEA selected from our ab initio simulations shows the TRIP-DP effect and exhibits higher ultimate tensile strength as well as strain-hardening ability compared to the corresponding equiatomic CoCrFeMnNi alloy. Our study reveals the improved mechanical properties achievable by introducing the TRIP-DP effect into HEAs and that ab initio calculations provide a powerful tool to screen the large compositional space to find potential candidate alloys.

Acknowledgements

This work is financially supported by the European Research Council under the EU's 7th Framework Programme (FP7/2007-2013)/ERC grant agreement 290998. F.K. acknowledges funding via the scholarship KO 5080/1-1 of the Deutsche Forschungsgemeinschaft (DFG). The authors would like to gratefully acknowledge the kind support of H. Springer, M. Adamek, B. Breitbach, M. Nellessen, F. Schlüter, F. Rütters and J. Wichert at the Max-Planck-Institut für Eisenforschung.

References

[1] J.W. Yeh, S.K. Chen, S.J. Lin, J.Y. Gan, T.S. Chin, T.T. Shun, C.H. Tsau, S.Y. Chang, Nanostructured high-entropy alloys with multiple principal elements: novel alloy design concepts and outcomes, Adv. Eng. Mater. 6 (2004) 299–303.
[2] Y. Zhang, T.T. Zuo, Z. Tang, M.C. Gao, K.A. Dahmen, P.K. Liaw, Z.P. Lu, Microstructures and properties of high-entropy alloys, Prog. Mater. Sci. 61 (2014) 1–93.
[3] M.C. Gao, J.-W. Yeh, P.K. Liaw, Y. Zhang, High-entropy Alloys: Fundamentals and Applications, Springer, 2016.
[4] B. Cantor, I.T.H. Chang, P. Knight, A.J.B. Vincent, Microstructural development in equiatomic multicomponent alloys, Mater. Sci. Eng. A 375–377 (2004) 213–218.
[5] B. Gludovatz, A. Hohenwarter, D. Catoor, E.H. Chang, E.P. George, R.O. Ritchie, A fracture-resistant high-entropy alloy for cryogenic applications, Science 345 (2014) 1153–1158.
[6] O.N. Senkov, J.M. Scott, S.V. Senkova, D.B. Miracle, C.F. Woodward, Microstructure and room temperature properties of a high-entropy TaNbHfZrTi alloy, J. Alloy. Compd. 509 (2011) 6043–6048.
[7] M. Feuerbacher, M. Heidelmann, C. Thomas, Hexagonal high-entropy alloys, Mater. Res. Lett. 3 (2014) 1–6.
[8] Y. Deng, C.C. Tasan, K.G. Pradeep, H. Springer, A. Kostka, D. Raabe, Design of a twinning-induced plasticity high entropy alloy, Acta Mater. 94 (2015) 124–133.
[9] F. Otto, A. Dlouhý, C. Somsen, H. Bei, G. Eggeler, E.P. George, The influences of temperature and microstructure on the tensile properties of a CoCrFeMnNi high-entropy alloy, Acta Mater. 61 (2013) 5743–5755.
[10] D.B. Miracle, O.N. Senkov, A critical review of high entropy alloys and related concepts, Acta Mater. 122 (2017) 448–511.
[11] C.C. Tasan, Y. Deng, K.G. Pradeep, M.J. Yao, H. Springer, D. Raabe, Composition dependence of phase stability, deformation mechanisms, and mechanical properties of the CoCrFeMnNi high-entropy alloy system, JOM 66 (2014) 1993–2001.
[12] K.G. Pradeep, C.C. Tasan, M.J. Yao, Y. Deng, H. Springer, D. Raabe, Non-equiatomic High entropy alloys: approach towards rapid alloy screening and property-oriented design, Mater. Sci. Eng. A 648 (2015) 183–192.
[13] Y.P. Wang, B.S. Li, H.Z. Fu, Solid solution or intermetallics in a high-entropy alloy, Adv. Eng. Mater. 11 (2009) 641–644.
[14] D. Ma, B. Grabowski, F. Körmann, J. Neugebauer, D. Raabe, Ab initio thermodynamics of the CoCrFeMnNi high entropy alloy: importance of entropy contributions beyond the configurational one, Acta Mater. 100 (2015) 90–97.
[15] Z. Li, K.G. Pradeep, Y. Deng, D. Raabe, C.C. Tasan, Metastable high-entropy dual-phase alloys overcome the strength–ductility trade-off, Nature 534 (2016) 227–230.
[16] Z. Li, C.C. Tasan, H. Springer, B. Gault, D. Raabe, Interstitial atoms enable joint twinning and transformation induced plasticity in strong and ductile high-entropy alloys, Sci. Rep. 7 (2017) 40704.
[17] J.-B. Seol, D. Raabe, P.-P. Choi, Y.-R. Im, C.-G. Park, Atomic scale effects of alloying, partitioning, solute drag and austempering on the mechanical properties of high-carbon bainitic–austenitic TRIP steels, Acta Mater. 60 (2012) 6183–6199.
[18] D. Raabe, C.C. Tasan, H. Springer, M. Bausch, From high-entropy alloys to high-entropy steels, Steel Res. Int. 86 (2015) 1127–1138.
[19] Z. Li, C.C. Tasan, K.G. Pradeep, D. Raabe, A TRIP-assisted dual-phase high-entropy alloy: grain size and phase fraction effects on deformation behavior, Acta Mater. 131 (2017) 323–335.
[20] D. Raabe, F. Roters, J. Neugebauer, I. Gutierrez-Urrutia, T. Hickel, W. Bleck, J.M. Schneider, J.E. Wittig, J. Mayer, Ab initio-guided design of twinning-induced plasticity steels, MRS Bull. 41 (2016) 320–325.
[21] A. Saeed-Akbari, J. Imlau, U. Prahl, W. Bleck, Derivation and variation in composition-dependent stacking fault energy maps based on subregular solution model in high-manganese steels, Metall. Mater. Trans. A 40 (2009) 3076–3090.
[22] T. Hickel, S. Sandlöbes, R.K.W. Marceau, A. Dick, I. Bleskov, J. Neugebauer, D. Raabe, Impact of nanodiffusion on the stacking fault energy in high-strength steels, Acta Mater. 75 (2014) 147–155.
[23] G. Frommeyer, U. Brüx, P. Neumann, Supra-ductile and high-strength manganese-TRIP/TWIP steels for high energy absorption purposes, ISIJ Int. 43 (2003) 438–446.
[24] O. Bouaziz, S. Allain, C.P. Scott, P. Cugy, D. Barbier, High manganese austenitic twinning induced plasticity steels: a review of the microstructure properties relationships, Curr. Opin. Solid State Mater. Sci. 15 (2011) 141–168.
[25] P.R. Thornton, T.E. Mitchell, P.B. Hirsch, The dependence of cross-slip on stacking-fault energy in face-centred cubic metals and alloys, Philos. Mag. 7 (1962) 1349–1369.
[26] S.L. Wong, M. Madivala, U. Prahl, F. Roters, D. Raabe, A crystal plasticity model for twinning- and transformation-induced plasticity, Acta Mater. 118 (2016) 140–151.
[27] D.T. Pierce, J.A. Jiménez, J. Bentley, D. Raabe, C. Oskay, J.E. Wittig, The influence of manganese content on the stacking fault and austenite/ε-martensite interfacial energies in Fe–Mn–(Al–Si) steels investigated by experiment and theory, Acta Mater. 68 (2014) 238–253.
[28] T. Hickel, B. Grabowski, F. Körmann, J. Neugebauer, Advancing density functional theory to finite temperatures: methods and applications in steel design,

J. Phys. Condens. Matter 24 (2012).
[29] B.S. Murty, J.W. Yeh, S. Ranganathan, High-entropy Alloys, Butterworth-Heinemann, 2014.
[30] F.Y. Tian, L.K. Varga, N.X. Chen, J. Shen, L. Vitos, Ab initio design of elastically isotropic TiZrNbMoVx high-entropy alloys, J. Alloy. Compd. 599 (2014) 19–25.
[31] F.Y. Tian, L.K. Varga, N.X. Chen, L. Delczeg, L. Vitos, Ab initio investigation of high-entropy alloys of 3d elements, Phys. Rev. B 87 (2013).
[32] F.Y. Tian, L. Delczeg, N.X. Chen, L.K. Varga, J. Shen, L. Vitos, Structural stability of NiCoFeCrAlx high-entropy alloy from ab initio theory, Phys. Rev. B 88 (2013).
[33] X. Li, F. Tian, S. Schonecker, J. Zhao, L. Vitos, Ab initio-predicted micro-mechanical performance of refractory high-entropy alloys, Sci. Rep. 5 (2015) 12334.
[34] A.J. Zaddach, C. Niu, C.C. Koch, D.L. Irving, Mechanical properties and stacking fault energies of NiFeCrCoMn high-entropy alloy, JOM 65 (2013) 1780–1789.
[35] S. Huang, W. Li, S. Lu, F. Tian, J. Shen, E. Holmström, L. Vitos, Temperature dependent stacking fault energy of FeCrCoNiMn high entropy alloy, Scr. Mater. 108 (2015) 44–47.
[36] L. Vitos, H.L. Skriver, B. Johansson, J. Kollár, Application of the exact muffin-tin orbitals theory: the spherical cell approximation, Comput. Mater. Sci. 18 (2000) 24–38.
[37] L. Vitos, Total-energy method based on the exact muffin-tin orbitals theory, Phys. Rev. B 64 (2001) 014107.
[38] L. Vitos, I.A. Abrikosov, B. Johansson, Anisotropic lattice distortions in random alloys from first-principles theory, Phys. Rev. Lett. 87 (2001) 156401.
[39] L. Vitos, Computational Quantum Mechanics for Materials Engineers: the EMTO Method and Applications, Springer Science & Business Media, 2007.
[40] P. Soven, Coherent-potential model of substitutional disordered alloys, Phys. Rev. 156 (1967) 809–813.
[41] B.L. Gyorffy, Coherent-potential approximation for a nonoverlapping-muffin-tin-potential model of random substitutional alloys, Phys. Rev. B 5 (1972) 2382–2384.
[42] J.P. Perdew, K. Burke, M. Ernzerhof, Generalized gradient approximation made simple, Phys. Rev. Lett. 77 (1996) 3865–3868.
[43] H.J. Monkhorst, J.D. Pack, Special points for Brillouin-zone integrations, Phys. Rev. B 13 (1976) 5188–5192.
[44] F. Körmann, D. Ma, D.D. Belyea, M.S. Lucas, C.W. Miller, B. Grabowski, M.H.F. Sluiter, "Treasure maps" for magnetic high-entropy-alloys from theory and experiment, Appl. Phys. Lett. 107 (2015) 142404.
[45] J. Staunton, B.L. Gyorffy, A.J. Pindor, G.M. Stocks, H. Winter, The "disordered local moment" picture of itinerant magnetism at finite temperatures, J. Magn. Magn. Mater. 45 (1984) 15–22.
[46] B.L. Gyorffy, A.J. Pindor, J. Staunton, G.M. Stocks, H. Winter, A first-principles theory of ferromagnetic phase transitions in metals, J. Phys. F. Met. Phys. 15 (1985) 1337.
[47] V.L. Moruzzi, J.F. Janak, K. Schwarz, Calculated thermal properties of metals, Phys. Rev. B 37 (1988) 790–799.
[48] Z. Li, D. Raabe, Influence of compositional inhomogeneity on mechanical behavior of an interstitial dual-phase high-entropy alloy, Mater. Chem. Phys. (2017), http://dx.doi.org/10.1016/j.matchemphys.2017.1004.1050.
[49] S. Zaefferer, N.-N. Elhami, Theory and application of electron channelling contrast imaging under controlled diffraction conditions, Acta Mater. 75 (2014) 20–50.
[50] B. Schuh, F. Mendez-Martin, B. Völker, E.P. George, H. Clemens, R. Pippan, A. Hohenwarter, Mechanical properties, microstructure and thermal stability of a nanocrystalline CoCrFeMnNi high-entropy alloy after severe plastic deformation, Acta Mater. 96 (2015) 258–268.
[51] J.W. Brooks, M.H. Loretto, R.E. Smallman, Direct observations of martensite nuclei in stainless steel, Acta Metall. 27 (1979) 1839–1847.